AALBORG UNIVERSITY

A compact 3-DOF shoulder mechanism constructed with scissors linkages for exoskeleton applications

Castro, Miguel Nobre; Rasmussen, John; Andersen, Michael Skipper; Bai, Shaoping

A compact 3-DOF shoulder mechanism constructed with scissors linkages for exoskeleton applications

Miguel Nobre Castro[a,1](✉), John Rasmussen[a,2], Michael Skipper Andersen[a,3], Shaoping Bai[a,4]

Department of Materials and Production, Aalborg University, Aalborg East, Denmark
[1]mnc@mp.aau.dk, [2]jr@mp.aau.dk, [3]msa@mp.aau.dk, [4]shb@mp.aau.dk

Corresponding Author: (✉) Miguel Nobre Castro

Abstract
A novel 3-degrees-of-freedom (DOF) spherical mechanism, singularity-free in the anatomical shoulder joint workspace, is described. The use of curved scissors linkages interconnected by revolute joints, whose axes share the same remote centre-of-motion, achieves the most compact design of its kind. The kinematics of this scissors shoulder mechanism (SSM) are derived and presented. A design equation restricting the linkage's curvature by the central/pitch angle of the fully stretched scissors is obtained. Motion-captured data are used for validating the reachable 3-d workspace while a test-subject is wearing a null protraction/retraction constrained exoskeleton. The embodiment of the SSM as a shoulder joint for an exoskeleton device does not compromise the upper extremity function within the anatomical reachable 3-d workspace. It operates within a volume of 0.236 m^3, corresponding to 68.09% and 94.97% of the volumes of the full active (0.350 m^3) and null protraction/retraction constrained active (0.223 m^3) reachable workspaces of the test-subject, respectively. Thus, the SSM represents a simplification of a spatial spherical mechanism design and overcomes the need for the use of redundant links and optimization routines.

Keywords
Scissors spherical mechanism, Compact shoulder mechanism; Scissors linkages; Kinematics; Exoskeleton; Reachable Workspace.

1. Introduction

The need for spherical mechanisms and robotic spherical manipulators is increasing. The conventional industrial serial manipulators, composed of consecutive revolute joints, can work around an object but they often require a change of configuration when the robot approaches a singularity [1]. From that point, changing the configuration of a manipulator with straight links can be problematic, as it must be simultaneously ensured that the robot does not collide with objects. For this reason, the creation of serial spherical mechanisms with curved links is advantageous, as they work on a spherical surface around the object. Most of the spherical shoulders are composed of three perpendicular rotation axes (3R), thus behaving like a gimbal mechanism [2–4]. An inherent disadvantage of this class of mechanisms is locking in inevitable singular configurations. To avoid the complications related with the singularity, some improvements and workarounds were made in the past: for example, the use of extra/redundant linkages [5] and design optimization on linkages' lengths [6] were reported.

Spherical mechanisms are critically important for building an exoskeleton's shoulder joint, since it has to surround the anatomical shoulder structure while pairing with its motions. Since the anatomical shoulder joint is a spherical ball-and-socket joint itself, the surrounding biological structures (bones, muscles and skin) will occupy the workspace of the shoulder mechanism. Additionally, both joint centres must coincide to avoid discomfort [7]. Attempts were made to meet these requirements. In some works [2–4], the spherical serial mechanism was configured in such way that the singular configurations lie outside the anatomical reachable workspace. Lo and Xie [5] also suggested a 4R shoulder mechanism with the addiction of an extra revolute joint, but this extra joint creates kinematic redundancy. The double parallelogram mechanism proposed by Christensen and Bai [8] is able to produce singularity-free rotations in the anatomical shoulder joint workspace, which is a variation and a down-scaled version of the classic double parallelogram mechanism [9]. On the other hand, despite its singularity-free characteristic, the mechanism protrudes out of the shoulder region and its lack of compactness compromises its wearability, which is usually a challenging and relevant design feature in these devices [10,11].

In this work, we attempt to achieve a mechanism which is both singularity-free in the anatomical shoulder joint workspace and as compact as a serial spherical mechanism by means of scissors with curved linkages. The traditional scissors mechanism can be found in lifting and tongue mechanisms [9] and has also been used to generate deployable spatial structures [12,13]. A famous case is the one proposed by Charles Hoberman, a radially deploying structure, which resulted in a well-known children's toy, the Hoberman Sphere [14]. A few years ago, the use of curved scissors linkages in a so called "symmetrical parallelogram mechanical network" was presented by Kocabas [15] as a 1-DOF gripper mechanism. Other authors, Watson et al. [16], also referred to these as spherical pantographs. To the authors' knowledge, the extension of curved scissors linkages to a spatial shoulder joint has never been explored.

In this paper, a novel serial spherical scissors mechanism with crossing, curved linkages is proposed and described. Its kinematics are derived and the respective manipulability measure will be used to evaluate the performance of the mechanism and eventual singular points in its workspace. An application case of the mechanism as a spherical joint for an upper extremity exoskeleton is presented. The device's performance

is evaluated by experimentally measuring the reachable 3-D workspace on a participant while wearing and not wearing a real prototype. The paper will be concluded with the discussion of these results.

2. Mechanism Kinematics
2.1. Conceptual development

The anatomical shoulder complex is an intricate joint which is mainly capable of performing three rotations (flexion/extension, internal/external rotation and abduction/adduction) about three different axis perpendicular to three distinct planes and has two translation directions (elevation/depression and protraction/retraction), as exemplified in Figure 1. Designing mechanical shoulder joints that are singularity-free in the anatomical shoulder joint workspace is a problem that has been addressed repeatedly, either by repositioning the axes of the typical curved serial linkages shoulder configuration or by using redundant linkages. The problem for one particular case was comprehensively dissected by Lo and Xie [17]. For the configuration presented in Figure 2-A, the existing singularity of the system coincides with the posture of a 90º shoulder flexion as represented in Figure 2-B. At this singularity point, the mechanism's internal/external rotation axis aligns with its abduction/adduction axis, resulting in the loss of a DOF. The practical consequence is that the mechanism no longer allows shoulder movements in the direction of abduction/adduction, hence compromising its functionality.
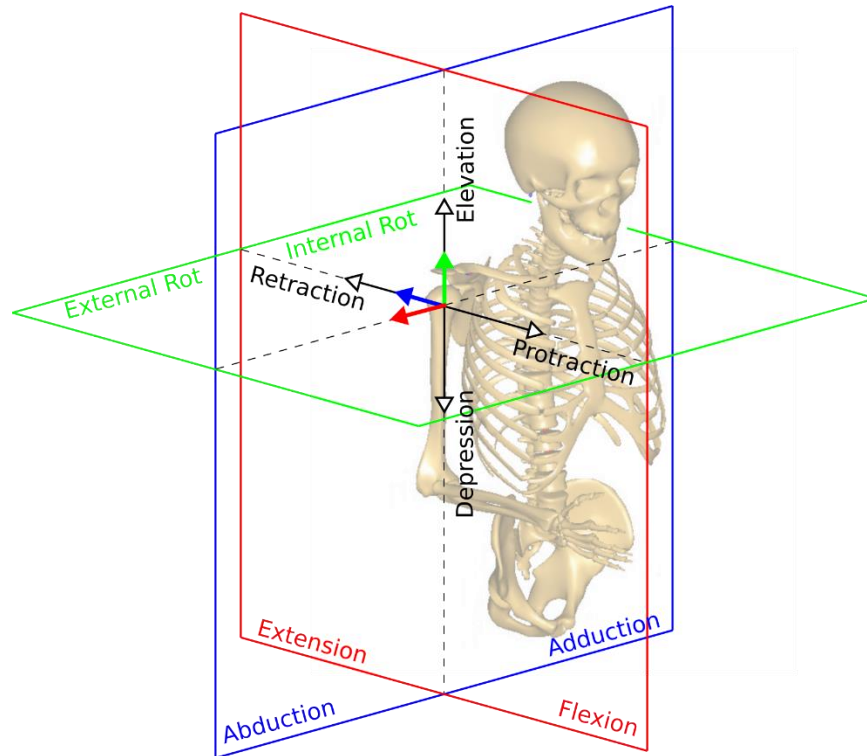

Figure 1. The anatomical shoulder complex is capable of three rotations about three different axis perpendicular to three distinct planes (colored planes) and two translation movements (black arrows).

To solve this singularity problem, an attempt was made to create a similar mechanism with the exact same rotational properties but without the kinematic constraint imposed by the singularity. Taking Figure 2-B as the starting point, it is possible to substitute the first curved link of the shoulder mechanism by a sliding element such that enables avoiding the singularity problem when the arm attains a 90 degree shoulder flexion. Such a sliding element was designed as a rhombus mechanism, as shown in Figure 2-C, and it allows the abduction/adduction movements to be performed. The introduction of this rhombus mechanism results in the addition of an extra revolute joint in the spherical joint, which allows removal of the very last of the original joints (along the longitudinal axis of the arm) given its redundancy as depicted in the final Figure 2-D.
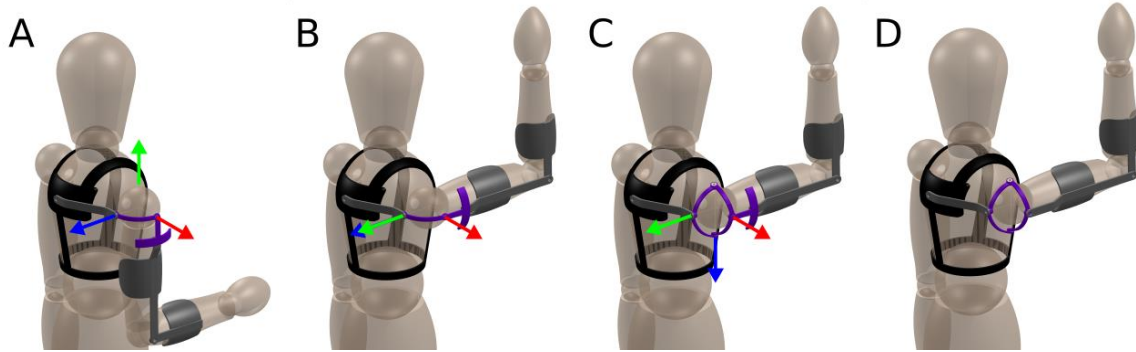

Figure 2. (A) The original configuration of the spherical shoulder mechanism discussed by Xo & Lie [17]; (B) The posture in which the configuration presents a singularity with a loss of a DOF as result of the alignment between the mechanism's internal/external rotation axis (green arrow) and its abduction/adduction axis (blue arrow). (C) By introducing the first linkage in the joint by the simplest spherical scissor mechanism (one rhombus), the mechanism recovers the missing DOF. (D) The original sliding mechanism corresponding to the third rotation axis, longitudinal to the segment, then becomes redundant.

The obtained spherical joint is, however, still not useful in the context of an exoskeleton due to the interference of the edges in the big diagonal with both musculatures of the arm and of the clavicle region when the mechanism is collapsed. Figure 3-A illustrates this problem. The solution is presented in Figure 3-B as the single rhombus is discretized into smaller rhombi as it will be explained in the following section.

2.2. The scissors shoulder mechanism

Curved linkages with known, constant curvature (fixed radius), will make all linkages of the rhombus move on a spherical surface, as illustrated in Figure 4. This occurs since all revolute joints' axes share a common remote centre-of-motion (RCM). In a spherical mechanism, a link is characterized by its great circle arc – i.e. the geodesic – between two joints at the sphere centre [18]. Thus, this spherical shoulder mechanism with three DOF will be hereinafter designated as the scissors shoulder mechanism (SSM)[1]. One of its key features is that its linkages lay and move always on a spherical surface with a pre-defined

---

[1] The mechanism has been also named as 'CXD', short for Compact X-scissors Device.

radius, which is essential to the achievement of a compact design in a spherical shoulder mechanism.
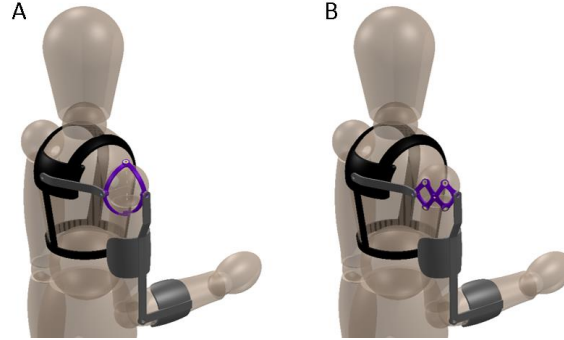

Figure 3. (A) The configuration of the spherical scissor mechanism with one rhombus still interferes with the upper arm anatomy by penetrating within its volume; (B) Therefore, the initial single rhombus can be discretized in smaller rhombi, in this case two rhombi.

Kinematically, the SSM is equivalent to a serial manipulator. This makes the modelling of the mechanism straightforward. Figure 4 shows the setup of coordinate systems and motion parameters of the three rotations on a single and simplified rhombus.

In the case of multiple rhombi composing the SSM as exemplified in Figure 5, the smallest linkages have one half of the arc length, which is defined as the product between the linkage curvature angle and the spherical radius, while the longer crossing linkages maintain their original arc length. This can be of importance in assemblies where it is desired to minimize the spherical area occupied by the mechanism, i.e. the total area enclosed by the linkages. In comparison, the area enclosed by the linkages of both rhombi ABCD and DEFG shown in Figure 5 represents half of that enclosed by the linkages of the rhombus ABCD shown in Figure 4.

The kinematics of many spherical mechanisms were previously presented [19]. The derivation of the kinematics of a similar spherical gripper mechanism was presented by Kocabas [15] using a set of projection angles to describe the mechanism's capability of grabbing objects. A new kinematic formulation for this SSM will be derived for the simpler single rhombus version, showing the ease of driving this mechanism from its base joint like a pure spherical shoulder mechanism.

2.2.1.Forward Kinematics

To model the single rhombus shown in Figure 4, the RCM was chosen as the common origin for all reference frames of the links comprising the mechanism. This helps simplifying the use of a Denavit-Hartenberg [20] angle convention for lower-pairs since radial distances and elevation parameters are not included. According to Ouerfelli and Kumar [21], the spherical mechanism with a closed loop is separated into two distinct chains: an upper and a lower chain with even and odd indexing, respectively. That said, the inter-linkage joint angles set φ_i and the associated linkages' twist/curvature angles α_{i-1} are presented for the upper chain linkages II and IV of the SSM in Figure 6 and in Table 1. An extra linkage six is added to represent the rotations of an end-effector link. The z-axis

of the reference frame in each linkage points along its proximal revolute joint axes while the x-axis points to the left, perpendicularly to the great circle where that linkage lies (denoted by the dashed lines in Figure 6).
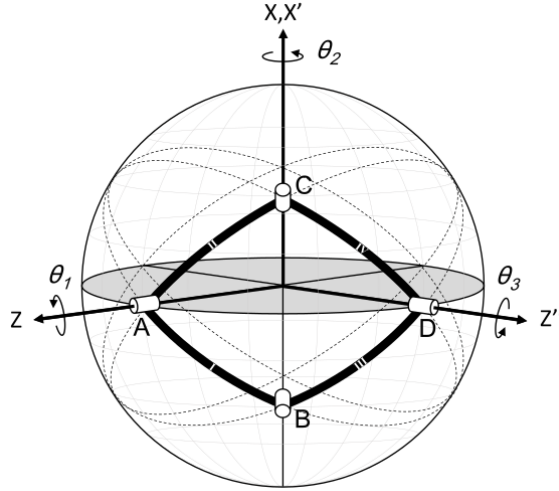

Figure 4. The principle of the novel SSM – a spherical mechanism. Each linkage describes a great circle arc, between two revolute joints, on a spherical surface. The mechanism rotations are described by the Euler angles of Z-X-Z convention: θ_1, θ_2 and θ_3, respectively.

Table 1. Denavit-Hartenberg parameters of the SSM.

Link	α_{i-1}	φ_i
I	0	φ_1
II	0	φ_2
IV	α	$-\varphi_2$
VI	α	φ_6

The rotation matrix $\mathbf{R_e}$, corresponding to the transformation from the end-effector coordinates to the global reference frame, is readily obtained as

$$\mathbf{R_e} = \mathbf{R_Z}(\varphi_1)\mathbf{R_Z}(\varphi_2)\mathbf{R_X}(\alpha)\mathbf{R_Z}(-\varphi_2)\mathbf{R_X}(\alpha)\mathbf{R_Z}(\varphi_6) \tag{1}$$

$\mathbf{R_e}$ can also be found by resorting to three sequential rotations with three Euler angles θ_j following the ZXZ-angle convention. This is valuable to relate the scissors' internal angle φ_2 with the pitch angle θ_2 of the end-effector of the manipulator. Hence, two of the relations can be directly derived from known angular quantities shown in Figure 6, while the third relation can be obtained from the spherical law of cosines shown in Equation (2).

$$\cos\theta_2 = \cos^2\alpha + \sin^2\alpha\cos(\pi - \varphi_2) \tag{2}$$

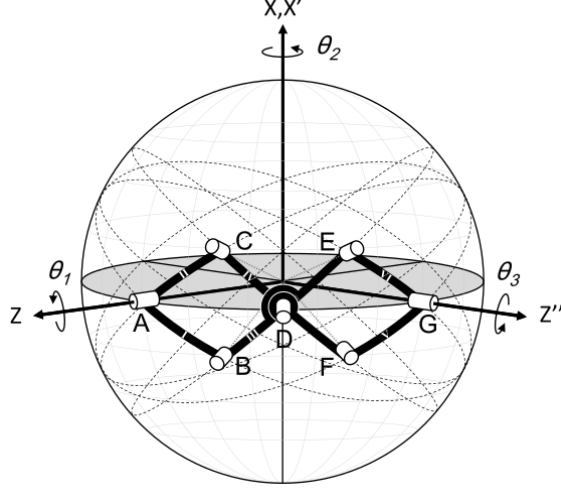These relations are described through Equations (3), (4) and (5).

Figure 5. A SSM constructed with two rhombi/scissors. This enables decreasing the spherical surface occupied by the mechanism, which can be advantageous in some situations.

$$\theta_1 = \varphi_1 + \frac{\varphi_2}{2} \tag{3}$$

$$\theta_2 = \arccos(\cos^2 \alpha - \sin^2 \alpha \cos \varphi_2) \tag{4}$$

$$\theta_3 = \varphi_6 - \frac{\varphi_2}{2} \tag{5}$$

Finally, rotation matrix $\mathbf{R}_e$ entries are presented in the following Equation (6),

$$\mathbf{R}_e = \mathbf{R}_Z(\theta_1)\mathbf{R}_X(\theta_2)\mathbf{R}_Z(\theta_3) =$$
$$\begin{bmatrix} c\,\theta_1\,c\,\theta_3 - s\,\theta_1\,c\,\theta_2\,s\,\theta_3 & -c\,\theta_1\,s\,\theta_3 - s\,\theta_1\,c\,\theta_2\,c\,\theta_3 & s\,\theta_1\,s\,\theta_2 \\ s\,\theta_1\,c\,\theta_3 + c\,\theta_1\,c\,\theta_2\,s\,\theta_3 & -s\,\theta_1\,s\,\theta_3 - c\,\theta_1\,c\,\theta_2\,c\,\theta_3 & -c\,\theta_1\,s\,\theta_2 \\ s\,\theta_2\,s\,\theta_3 & s\,\theta_2\,c\,\theta_3 & c\,\theta_2 \end{bmatrix} \tag{6}$$

where $c\theta_j$ and $s\theta_j$ correspond to the cosine and sine functions of a θ_j angle, respectively.
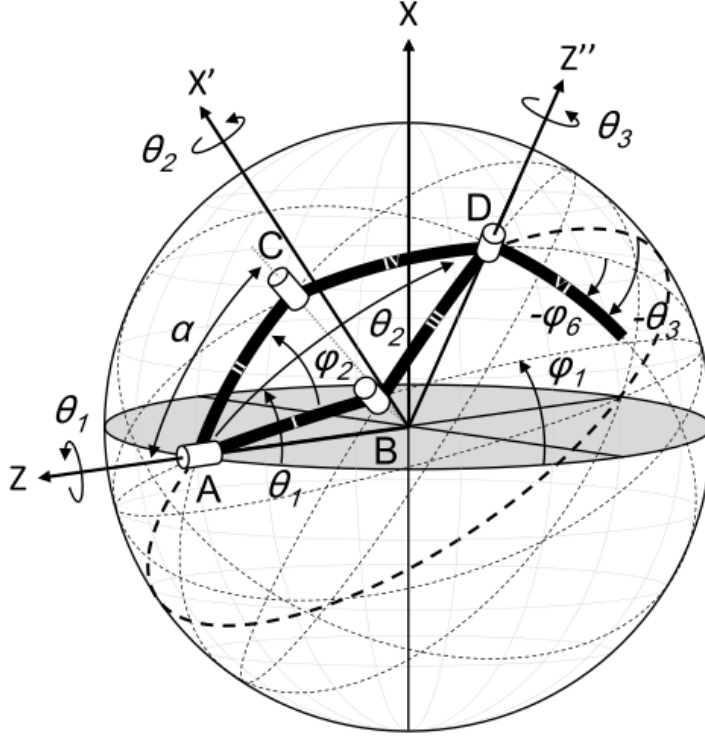
Figure 6. Description of the SSM in terms of the inter-linkages angles. Two angles sets can help describing the kinematics of the mechanism: the inter-linkage joint angles set φ_i and an Euler angles set θ_j following the ZXZ-angle convention. A curvature angle α is associated to each linkage.

Figure 7 shows the scissors' internal angle φ_2 with the pitch angle θ_2 of the end-effector (the most distant vertex of the scissors), where an inverse proportionality between the pitch angle θ_2 and scissors' internal angle φ_2 can be observed. Moreover, for a closed and stretched scissors ($\varphi_2 = 0°$), the pitch angle θ_2 is twice that of the curvature angle α corresponding to the arc length of each linkage.

Figure 7. End-effector pitch angle θ_2 - internal scissors angle φ_2 relationship for different values of links curvature angle. On a single rhombus SSM, for a given curvature angle curvature angle α corresponds a pitch angle θ_2 with twice its value.
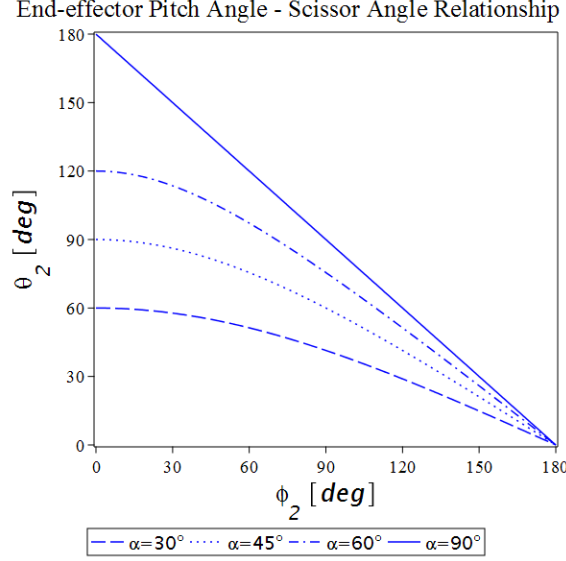
2.2.2. Inverse Kinematics

The inverse problem consists of computing the three Euler angles θ_j from a given final positions of the end-effector of the manipulator. This can be achieved by initially calculating the value of the pitch angle θ_2 directly from the last entry of the rotation matrix $\mathbf{R_e}$ as in Equation (7). The r_{ij} represents the matrix element in the ith row and j^{th} column. Since the mechanism operates in the range of $\theta_2 \in [0, 2\alpha]$, only the positive angle from Equation (7) is of interest.

$$\cos\theta_2 = r_{33} \tag{7}$$

Once the pitch angle θ_2 is known, the remaining elements in the last row and last column of the rotation matrix $\mathbf{R_e}$ can be paired in terms of the remaining θ_1 and θ_3 angles and trivially obtained by the geometrical tangent function as in Equations (8) and (9).

$$\theta_1 = \arctan2(r_{13}/s\,\theta_2, -r_{23}/s\,\theta_2) \tag{8}$$
$$\theta_3 = \arctan2(r_{31}/s\,\theta_2, r_{32}/s\,\theta_2) \tag{9}$$

Upon these solutions, the mechanism's joint angles φ_i can be obtained using Equations (3), (4) and (5).

2.2.3. Manipulability Analysis

A manipulator's Jacobian matrix $\mathbf{J(\theta)}$ relates the mechanism's joint velocities $\dot{\mathbf{\theta}}$ with the angular velocity $\mathbf{\omega_e}$ of its last reference frame, i.e. the angular velocity of its end-effector

9

$$\boldsymbol{\omega}_e = \mathbf{J}(\boldsymbol{\theta})\,\dot{\boldsymbol{\theta}} \tag{10}$$

where the generalized velocity vector is $\dot{\boldsymbol{\theta}} = [\dot{\theta}_1 \quad \dot{\theta}_2 \quad \dot{\theta}_3]^T$, and the end-effector angular-velocity vector is $\boldsymbol{\omega}_e = [\omega_x \quad \omega_y \quad \omega_z]^T$.

According to Euler's rotation theorem, any sequence of rotations can be described by a unit vector $\hat{\mathbf{k}}$ – the instantaneous axis of rotation – which is then scaled by the amount of rotation θ about that same axis. The theorem can then be extended such that, at any time instant, the angular-velocity vector $\boldsymbol{\omega}_e$ is equal to the speed of rotation $\dot{\theta}$ about that same instantaneous axis of rotation $\hat{\mathbf{k}}$ – see equation (11).

$$\boldsymbol{\omega}_e = \dot{\theta}\hat{\mathbf{k}} \tag{11}$$

Likewise, the angular-velocity vector $\boldsymbol{\omega}_e$ can be derived from the skew-symmetric matrix $\boldsymbol{S}$ of the angular-velocities for the particular rotation matrix $\mathbf{R}_e$ of the mechanism [22]. This is achieved by solving the matrix Equation (12), which corresponds to the three independent Equations (13), (14) and (15).

$$\boldsymbol{S} = \dot{\mathbf{R}}_e \mathbf{R}_e^T = \begin{bmatrix} 0 & -\omega_z & \omega_y \\ \omega_z & 0 & -\omega_x \\ -\omega_y & \omega_x & 0 \end{bmatrix} \tag{12}$$

$$\omega_x = \dot{r}_{31}r_{21} + \dot{r}_{32}r_{22} + \dot{r}_{33}r_{23} \tag{13}$$

$$\omega_y = \dot{r}_{11}r_{31} + \dot{r}_{12}r_{32} + \dot{r}_{13}r_{33} \tag{14}$$

$$\omega_z = \dot{r}_{21}r_{11} + \dot{r}_{22}r_{12} + \dot{r}_{23}r_{13} \tag{15}$$

By solving these equations for the generalized velocity vector $\dot{\boldsymbol{\theta}}$, it is then possible to obtain the following Jacobian matrix $\mathbf{J}(\boldsymbol{\theta})$ for the mechanism – Equation (16).

$$\mathbf{J}(\boldsymbol{\theta}) = \begin{bmatrix} 0 & c\,\theta_1 & s\,\theta_1\,s\,\theta_2 \\ 0 & s\,\theta_1 & -c\,\theta_1\,s\,\theta_2 \\ 1 & 0 & c\,\theta_2 \end{bmatrix} \tag{16}$$

The manipulability, $w(\boldsymbol{\theta})$, accesses whether the maximum rank of the Jacobian matrix is, at a given point, lower than the number of DOFs of the mechanism [23]. For this spherical joint, the manipulability is found as

$$w(\boldsymbol{\theta}) = \sqrt{\det(\mathbf{J}(\boldsymbol{\theta})\mathbf{J}^T(\boldsymbol{\theta}))} = |\det(\mathbf{J}(\boldsymbol{\theta}))| = |s\,\theta_2| \tag{17}$$

For the sake of enabling actuation of this mechanism in future applications, the manipulability can also be expressed in terms of the inter-linkages angles φ and linkage curvature angle α, i.e. $w(\boldsymbol{\varphi}, \alpha)$. This can be quickly achieved by recursively deriving the Jacobian matrix $\mathbf{J}(\boldsymbol{\varphi}, \alpha)$ in the end-effector frame, by propagating the angular velocity from link to link [22]. Thus,

$$^e\boldsymbol{\omega}_e = [\mathbf{J_1}(\boldsymbol{\varphi}, \alpha) \quad \mathbf{J_2}(\boldsymbol{\varphi}, \alpha) \quad \mathbf{J_3}(\boldsymbol{\varphi}, \alpha)] \begin{bmatrix} \dot{\varphi}_1 \\ \dot{\varphi}_2 \\ \dot{\varphi}_6 \end{bmatrix} \tag{18}$$

where

$$\mathbf{J_1}(\boldsymbol{\varphi}, \alpha) = (\mathbf{R_Z}(\varphi_2)\mathbf{R_X}(\alpha)\mathbf{R_Z}(-\varphi_2)\mathbf{R_X}(\alpha)\mathbf{R_Z}(\varphi_6))^T \begin{bmatrix} 0 \\ 0 \\ 1 \end{bmatrix} \tag{19}$$

$$\mathbf{J_2}(\boldsymbol{\varphi}, \alpha) = \left(\mathbf{R_X}(\alpha)\mathbf{R_Z}(-\varphi_2)\mathbf{R_X}(\alpha)\mathbf{R_Z}(\varphi_6)\right)^T \begin{bmatrix} 0 \\ 0 \\ 1 \end{bmatrix} - \left(\mathbf{R_X}(\alpha)\mathbf{R_Z}(\varphi_6)\right)^T \begin{bmatrix} 0 \\ 0 \\ 1 \end{bmatrix} \tag{20}$$

$$\mathbf{J_3}(\boldsymbol{\varphi}, \alpha) = \begin{bmatrix} 0 \\ 0 \\ 1 \end{bmatrix} \tag{21}$$

Consequently, the following manipulability result is obtained

$$w(\boldsymbol{\varphi}, \alpha) = \sqrt{\det(\mathbf{J}(\boldsymbol{\varphi}, \alpha)\mathbf{J}^T(\boldsymbol{\varphi}, \alpha))} = |\det(\mathbf{J}(\boldsymbol{\varphi}, \alpha))| = |\mathrm{s}\,\varphi_2\,\mathrm{s}^2\,\alpha| \tag{22}$$

A vanishing manipulability implies a singular configuration. Apart from the trivial requirement imposed by the linkage curvature angle α, which must be greater than zero, both Equations (17) and (22) show that the singularities of the mechanism are only dependent on the SSM's rhombus angles, i.e. either on the pitch angle θ_2 or on the scissors' internal angle φ_2 depending on the chosen angle formulation. These occur at configurations where the first and last rotation axes are aligned as represented in Figure 8: the folded scissors configuration ($\theta_2 = 0°$, $\varphi_2 = 180°$) and the fully stretched scissors configuration ($\theta_2 = 180°$, $\varphi_2 = 0°$). In order to grant stability to the mechanism and create a minimum lever arm distance to facilitate the motion near the kinematic range limits, the following general design Equation (23) relating the maximum pitch angle θ_2^{max} with the chosen linkages' curvature angle α and the n number of rhombi in the mechanism has been derived.

$$\theta_2^{max} = 2\alpha n < 180°, \ n \in \mathbb{N} \tag{23}$$

2.2.4. Practical Design Considerations

From a practical point-of-view, the joint and linkages of the mechanism do not behave as point or line entities. This means that, on a real manufactured mechanism, material exists around each joint axis, for example to accommodate bearings. The bearings themselves occupy some of the effective spherical surface on which the mechanism works. As illustrated in Figure 9, as the mechanism reaches its singular configurations, the boundaries of the parts composing the SSM will collide. This naturally occurs for both situations mentioned above, of the most folded and most stretched scissors configurations. An intrusive angle β is defined as the angle from the joint axis C to an imaginary axis M passing through the collision point. This spherical triangle ACM allows defining the real mechanism's angular limits in its most stretched configuration by the spherical law of cosines as in Equation (2). Since the cosine of the right angle at the vertex M is zero, the spherical law of cosines is simplified to Equation (24).
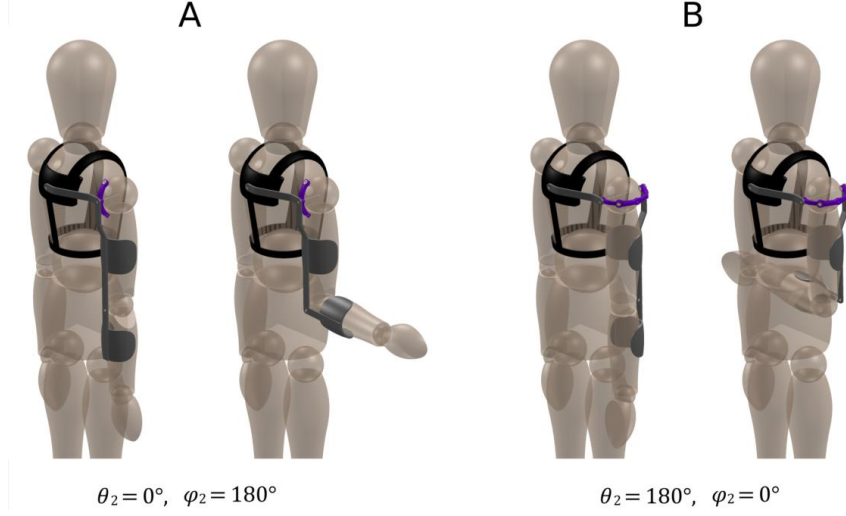
$\theta_2 = 0°, \quad \varphi_2 = 180°$ $\theta_2 = 180°, \quad \varphi_2 = 0°$

Figure 8. The two singular configurations obtained from the manipulability analyses for the SSM: (A) the folded and (B) the stretched scissors configurations. These correspond to 90° of shoulder external rotation and to 90° of shoulder internal rotation, respectively.

$$\cos \theta_2' = \cos \alpha / \cos \beta \qquad (24)$$

where θ_2' represents the portion of the scissors' pitch angle spanned between the mechanism's base joint axis A and the tangential imaginary axis M from which the intrusive angle β is measured. Thus, the maximum pitch angle is effectively $\theta_2^{max} = 2n\theta_2'$. On the other hand, by reasoning on the same intrusive angle β for the most folded configuration, the minimum pitch angle is $\theta_2^{min} = 2n\beta$. Such mechanical stop arises from design constraints imposed by housing bearings and grants stability by providing a small lever arm distance, which is suitable for facilitating the motion of shoulder mechanisms.

3. Prototype design and development
3.1. Design of an exoskeleton shoulder

As arm assistive devices run in parallel with the human body segments, they must not violate the physical constraints imposed by the anatomical shape of the user, and they must be kinematically compatible with the natural motions of the human, else they can cause discomfort or limit the range-of-motion of the user. As illustrated in the preceding section, constraints of the folded configurations may also limit the range-of-motion beyond the theoretical limits. These considerations call for prototype tests, which are performed in experiments.

A exoskeleton prototype (see Figure 10) was designed with the specifications mentioned in Table 2. A small intrusive centre angle $\beta = 8°$ generated around each axis for housing bearings prevents the mechanism from reaching any of the singular points. The SSM can fold to a minimum pitch angle of $\theta_2 = 32°$ and extend to a maximum pitch angle of $\theta_2 = 136°$. These enables 58° of external shoulder rotation and 46° of internal shoulder rotation, respectively. The designed exoskeleton has a total of five DOFs, thus allowing for shoulder elevation (one DOF), three shoulder rotations provided by the SSM (three DOFs) and elbow flexion (one DOF).
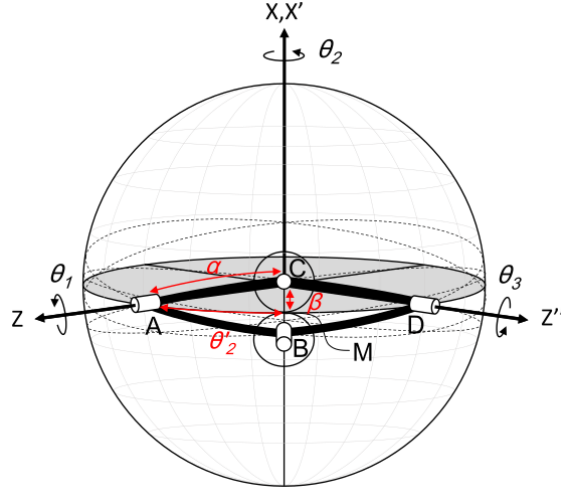
Figure 9. Maximum stretched configuration of the SSM illustrating the collision point between revolute joints' bearings represented by the two circular symbols. An intrusive angle β is defined as the angle from the joint axis to an axis M passing through that collision point. The spherical law of cosines applied to the triangle ACM enables relating β with α and θ_2'.

Figure 11 shows the SSM prototype with steel 3D-printed parts of curved links. The remaining parts of the exoskeleton were manufactured in aluminium. Once every part was assembled, the exoskeleton was tested on the subject.

Table 2. Specifications of the built SSM prototype.

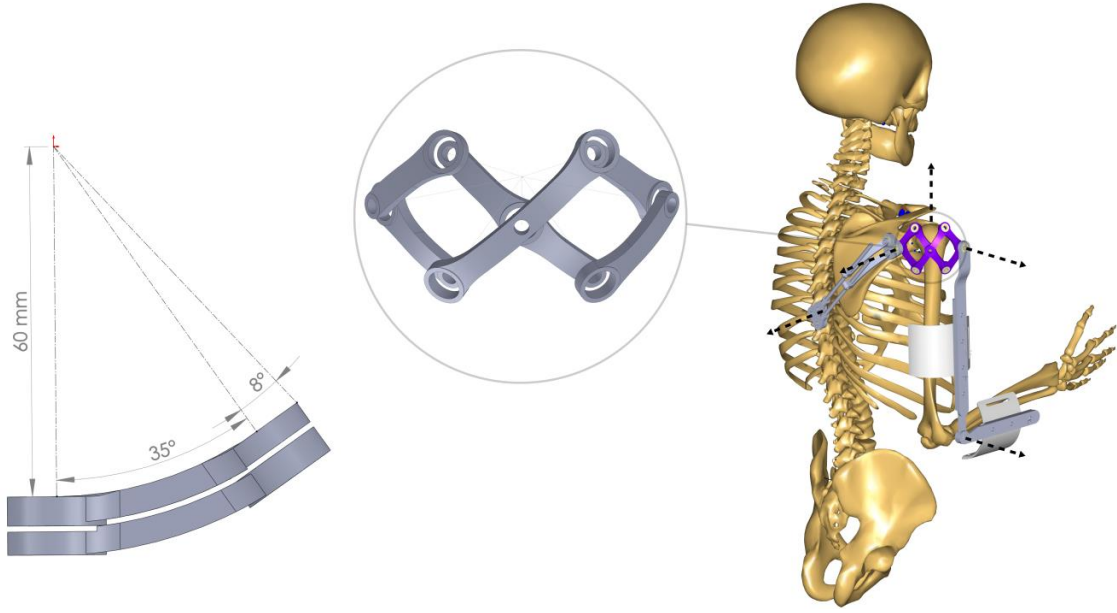|	
Sphere Radius	60 mm
Linkage curvature angle α	35°
Intrusive angle β	8°
Minimum SSM pitch angle θ_2 (shoulder external rotation)	32°
Maximum SSM pitch angle θ_2 (shoulder internal rotation)	136°

13

Figure 10. (Right) The lateral view of the curved linkage elements used in the built SSM prototype. The included specifications are: the inner sphere radius, linkage curvature angle α and intrusive centre angle β. (Left) CAD representation of the 5-DOF exoskeleton with the assembled SSM.

Figure 11. A detailed view of the steel 3-D printed version of the SSM prototype. On the right, a closer view of the mechanism when assembled on the manufactured version of the aluminum exoskeleton, while the latter is being worn.

3.2. Kinematic validation using the reachable 3-D workspace

An exoskeleton device is meant to assist or enhance strength of its user while performing common activities of the daily living (ADL). As it may not be feasible to test such device for every ADL, an alternative is to use the reachable 3-D workspace that gives a global approximation of the working ranges of the mechanism and can account for extreme cases too. Thus, the full anatomical reachable 3-D workspace was estimated based

14

on the five-tasks protocol created in our previous work, Castro et al. [24]. These five tasks are capable of capturing the close-to-torso (through the 'shower', 'curls' and 'free-motion' tasks) and far-from-torso (through the 'vertical' and 'horizontal' tasks) regions of the reachable 3-D workspace, allowing estimation of its envelope shape and volume. On top of that, given the distinct nature of these five-tasks, the upper extremity posture redundancy, with regards to the reachable 3-D workspace, is also captured. Hence, the AnyBody Modelling System v.6.1 (AnyBody Technology A/S, Aalborg, Denmark) software was used to model the upper extremity from the 'MocapModel' (AnyBody Managed Model Repository v.1.6.3). The full model comprised: a lumbar spine model, based on the work of De Zee et al. [25], and arm and shoulder models, based on the work of the Delft Shoulder Group [26–28]. In total, 7-DOF were allowed: three on the shoulder girdle, three on the shoulder joint and two on the elbow joint (flexion/extension and forearm pronation/supination). Wrist motions were disregarded and kept constant at neutral angles. The pelvis segment was fixed to the thorax such that both behaved as a single segment. The scapula was also kinematically constrained to slide on the surface of the rib cage.

To experimentally evaluate the reachable 3-D workspace, the test-subject was instrumented with reflective markers, according to the marker-set presented in [24] as exemplified in Figure 12. Firstly, all segments' length and hand breadth in the model were geometrically scaled to one test-subject (male, age 27, body mass 80 kg, height 1.75 m, upper-extremity length 0.642 m) from a static calibration trial using the method by Andersen et al. [29]. Afterwards, the participant was instructed to perform the five-tasks protocol for the kinematic assessment of the reachable workspace [24] three times: the first time consisted on recording the full active reachable workspace; keeping in mind the exoskeleton's mechanical constraint preventing shoulder protraction/retraction motion, the participant was instructed to perform the protocol a second time without protracting or retracting the shoulder (null angle); lastly, the protocol was performed while wearing the exoskeleton prototype. The recorded kinematic data was then used to drive the skeletal model by optimizing all model's marker trajectories as formulated by Andersen et al. [30].

Later, a point cloud set including all hand palm points (the end-effector of the upper extremity), for each of the two five-tasks protocols performed, was recorded relative to a thorax reference frame located on top of the sternum bone. The non-convex shaped envelopes of each of the three reachable workspaces were obtained resorting to the alpha-shape algorithm [31] according to the processing steps described on our previous work [24]. This algorithm works on a mesh of the point cloud as a "carving" sphere shaping its envelope and enables to capture its non-convex nature. Subsequently, the radius of that sphere was defined according to the convex shape of the human torso, which corresponds to the non-convex region of the envelope. Thus, such alpha-radius was defined as the semi-minor (smallest) radius of the cross-sectional area of the ellipsoid used to wrap the serratus anterior muscle around the thorax segment – as modelled by van der Helm et al. [26]: a value of 0.132 m was obtained in the case of this participant. The volumes of each reachable workspace's envelope were trivially calculated on MATLAB® (MathWorks, Natick, MA USA) and compared afterwards.

4. Experimental results

The participant's upper extremity reachable workspace point clouds and respective envelopes are presented below on Figure 13 and Figure 14. Without the exoskeleton, the volume obtained for the full active reachable workspace was 0.350 m^3 and when the shoulder protraction/retraction angle was forced to be zero, the volume decreased to 0.223 m^3. Once the participant worn the exoskeleton, the obtained reachable workspace volume was measured as 0.236 m^3. This value represents an intersection volume percentage of 68.09% in relation to the full active reachable workspace and a percentage of 94.97% in relation to the constrained active reachable workspace. Moreover, the shape difference and volume reduction observed in Figure 13 affects mostly the counter-lateral and frontal aspects of the full active reachable workspace.
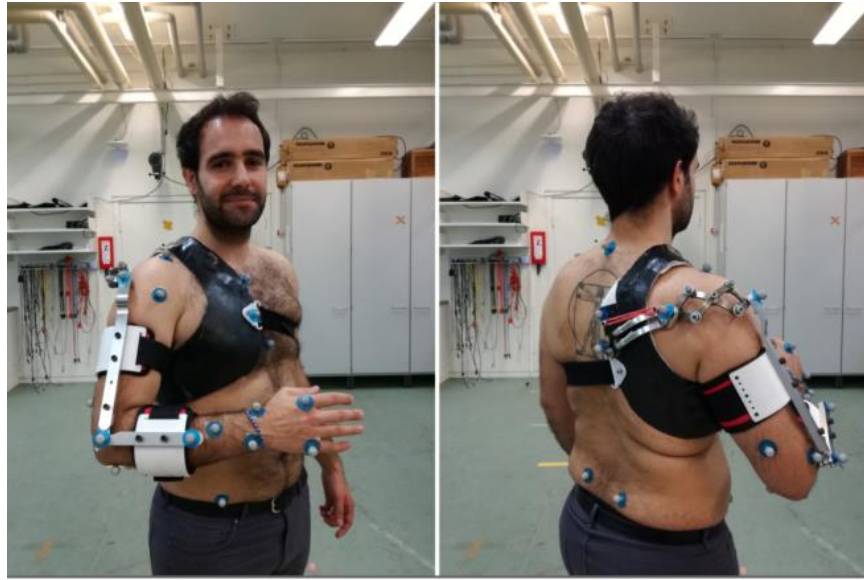

Figure 12. The reflective marker set presented in [24] for motion capture of the reachable workspace movement tasks while the subject was wearing and not wearing the exoskeleton with the SSM assembled.

5. Discussion

In this paper, a novel spherical SSM was described, highlighting its singularity-free characteristic in the anatomical shoulder joint workspace and its compactness as its linkages are constrained to a spherical surface with pre-defined radius. The mechanism's forward and inverse kinematics were derived and it was found that the mechanism comprises the three typical yaw-pitch-roll rotation axes known from gimbal mechanisms, but it is practically singularity-free. Moreover, the analysis of the performance of the mechanism through a manipulability metric enabled also to discover that there are only two configurations in which the SSM reaches a singularity: both when the scissors mechanism is completely folded or completely stretched. Nevertheless, the SSM can theoretically nearly work in the full spherical surface. A design constraint equation was derived to describe and detect the fully stretched scissors singularity. The design constraint states that the curvature angle α of the smallest of the linkages must be smaller than 90º divided by the number of rhombi/parallelograms in the mechanism. This finding agrees

16

with the previously reported by Kocabas [15] after the creation of a 1-DOF spherical gripper mechanism, also using scissors linkages.

The use of the SSM as a shoulder joint for an exoskeleton appears to be an improvement compared to what was previously presented in the literature. Lo and Xie [5] showed that most of the spherical serial mechanism's assemblies used to create valuable shoulder joints for exoskeletons cannot avoid singularities within the useful anatomical shoulder ROM. Most authors tend to work around the problem by moving the singularities to postures that are not reached very often [5–7] and the linkages of these serial spherical shoulders often have a curvature angle $\alpha = 90°$. Lo and Xie [5] also proposed the use of a redundant link through optimization. That leads afterwards to more required actuation. The SSM is therefore capable to overcome this limitation avoiding the computation expense inherent from that optimization step.
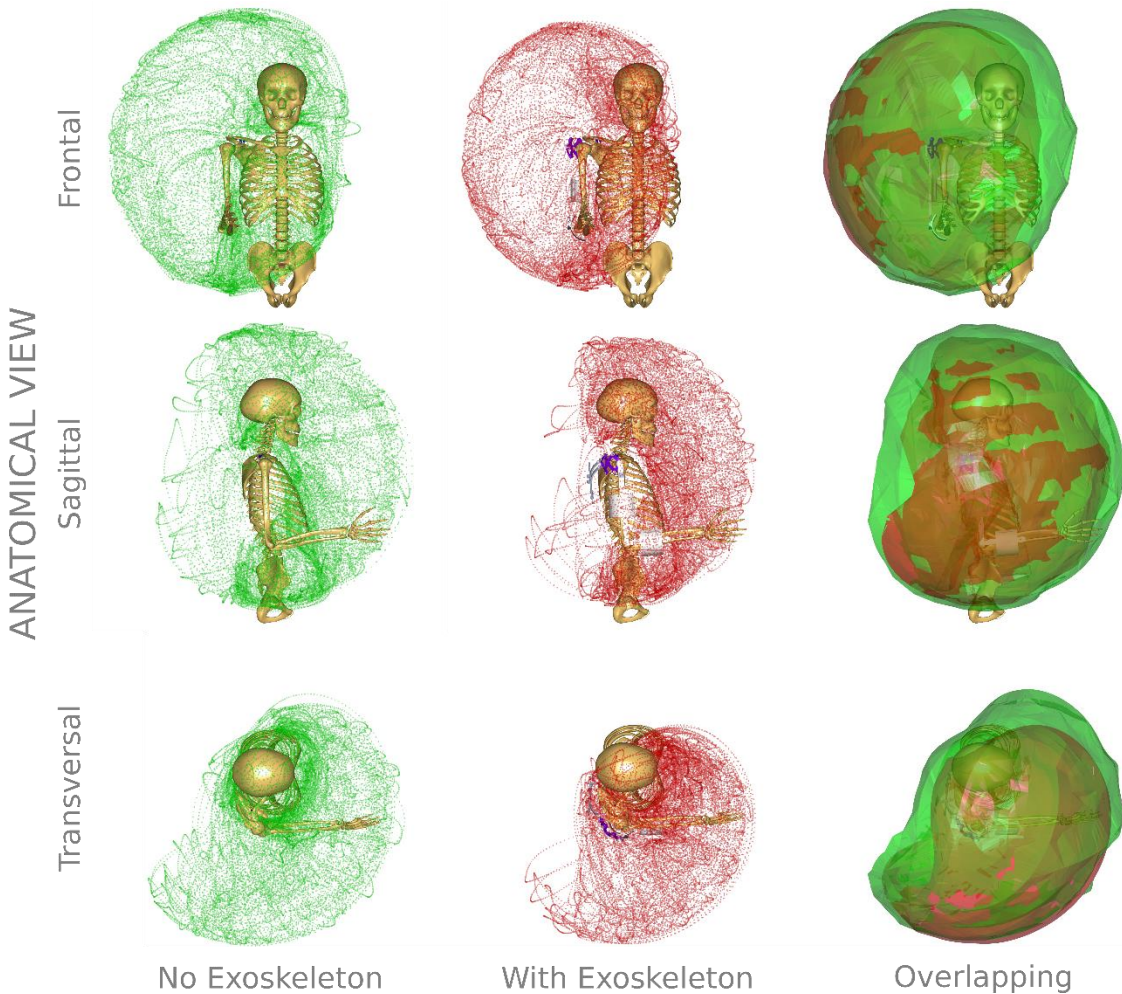

Figure 13. Comparison of the experimentally obtained reachable workspaces' point clouds and volumes while the participant was not wearing (green shape) and wearing (red shape) the exoskeleton. The obtained volumes were 0.350 m^3 and 0.236 m^3 respectively, corresponding to an intersection volume percentage of 68.09%.

Christensen and Bai [8] recently presented a double parallelogram shoulder mechanism which can equally solve that singularity problem. However, since exoskeletons are meant to be wearable [10,11], the protruding portion of the double parallelogram can now be eliminated by the use of the presented SSM. Thus, this work contributes with more wearability, compactness for lighter exoskeletons.

It is also important to mention that the only singularities in the human shoulder for this SSM with near full workspace occur both at 90° of shoulder internal ($\theta_2 \approx 180°$, $\varphi_2 = 0°$) and external ($\theta_2 = 0°$, $\varphi_2 = 180°$) rotations. The first is not attainable since it would mean penetrating the torso or performing an unusual maximal shoulder internal rotation, which resultant hand rotation can also be accomplished by pronating the forearm. The second corresponds to a point in the vicinity of the human upper extremity reachable workspace which is not within the 95th percentile maximum shoulder external rotation angle (55°) for healthy individuals [32]. After manufacturing and testing the prototype of the SSM it was possible to assess that is has a good fit to the shoulder anatomy. However, the mechanism still interferes with the collar bone while performing extreme shoulder abduction movements about the frontal (anatomical) plane. Whether this limitation is relevant depends on the application of the exoskeleton but it is not expected to cause issues as the exoskeleton enables the ROM required for common ADL [33]. Furthermore, the actual void spaces within the spherical area spanned by the SSM might need some shielding to avoid harming the user, for example, through finger impingement.

The manufactured prototype showed that having an intrusive angle, as described earlier, helps to avoid the fully folded and fully stretched scissors configurations, granting stability to the mechanism. The exclusive use of revolute joints may represent an advantage from a fabrication point-of-view, in the sense that revolute joints can be realised with standard bearings of low cost and high reliability. While common serial chain spherical shoulder manipulators inherently have low stiffness relative to the parallel ones [21,34], the presence of closed-loops in the scissors shoulder grants the mechanism a higher stiffness when compared to its purely serial relatives. Nevertheless, its stiffness when compared to a normal parallel spherical manipulator remains to be investigated. Another advantage of this mechanism is that, similarly to parallel spherical manipulators, it can be actuated from its base. Thus, it avoids the need for the proximal actuators to carry their distal counterparts.

The slight mismatch observed between volumes on Figure 13, more precisely the 68.09% intersection volume percentage, can be explained by the protraction/retraction DOF that the exoskeleton is missing, not enabling the test subject reaching that far. On top of that, it was later proven that removing such DOF from the active reachable workspace, as seen in Figure 14, leads to a 94.97% intersection volume percentage. Such phenomenon was previously observed by Schiele and van der Helm [35] while testing the reachable workspace of another wearable exoskeleton. Typically, such devices still compromise the complexity and all known DOFs of the shoulder girdle. However, even though the back and left hemispheres have reduced reachability, most activities of the daily living fall on the frontal hemisphere and when objects need to be manipulated on the left hemisphere, the left arm can cover that volume.
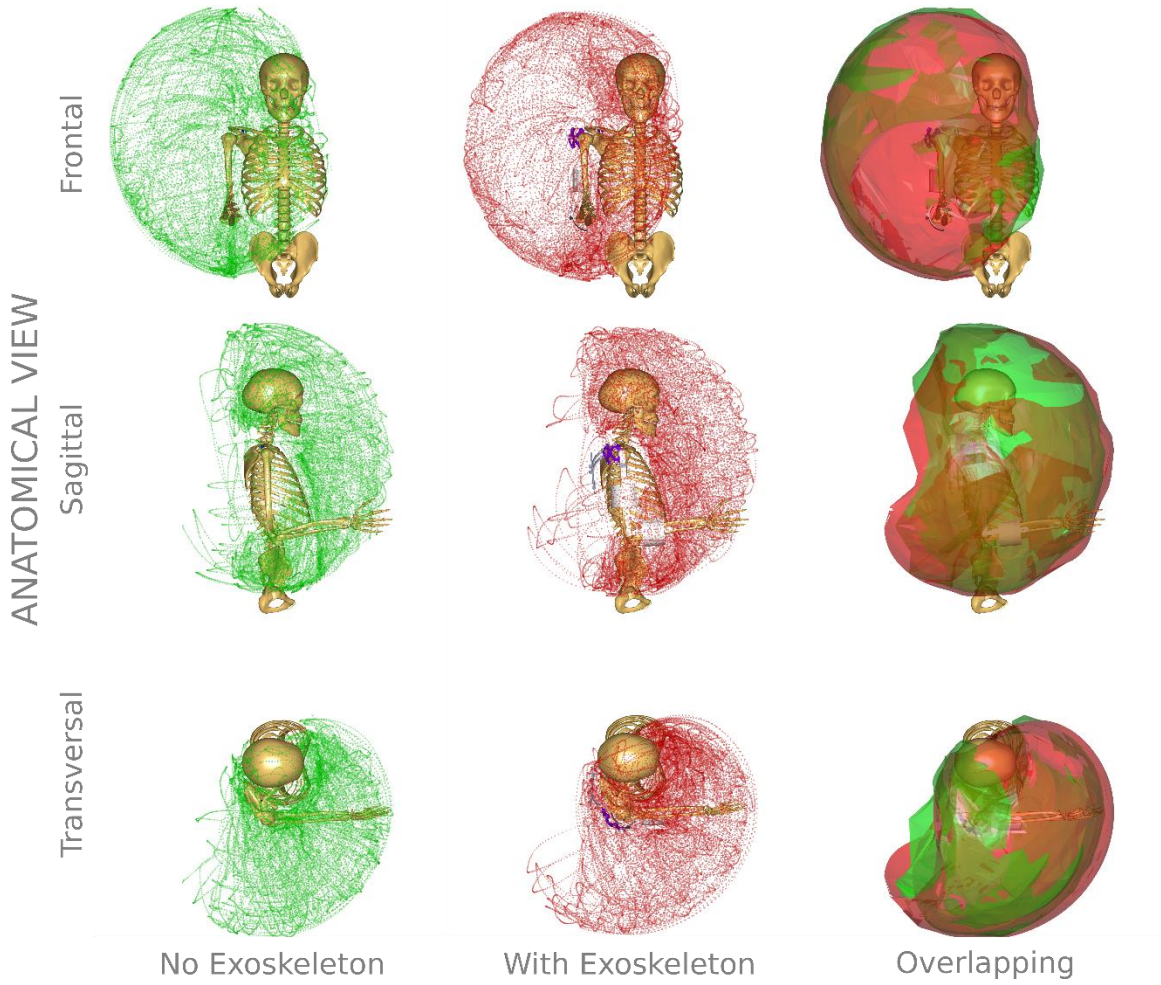
Figure 14. Comparison of the experimentally obtained reachable workspaces' point clouds and volumes while the participant was instructed to keep the shoulder protraction/retraction angle null without wearing the exoskeleton (green shape) and when freely moving the shoulder while wearing it (red shape). The obtained volumes were 0.223 m^3 and 0.236 m^3 respectively, corresponding to an intersection volume percentage of 94.97%.

Last but not least, it must be highlighted that the mechanism allows a spherical coordinate space, as opposed to the Cartesian coordinate space of most robotic manipulators. Besides exoskeleton applications, and as an extension of its functionality, a spherical coordinate positioning tool can be advantageous, for instance, in the medical field. The currently available robots for minimally invasive surgery tend to require large spaces [36]. Many of these surgery tools are required to be confined to a small space, such as that of an imaging scanner, when performing intraoperative navigation [37]. The spherical scissors shoulder can potentially provide a stiff surgical support tool which could otherwise only be achieved by larger, parallel robots. Other potential application areas of this mechanism are 3d-printing, haptic devices, laser welding/cutting tools and camera inspection structures for quality control, but all of these applications require further investigation.

6. Conclusion

In conclusion, the presented mechanism enables simplifying the design of spherical shoulder mechanisms by overcoming both the need for the use of redundant links or optimization routines. In its current state, the SSM can be used on a shoulder stabilizing brace for rehabilitating a traumatic dislocation or stroke-related subluxation of the shoulder, without requiring an actuation system. The mechanism is able to hold the humerus bone head in place as the upper extremity moves. With regards to the exoskeletons research field, its compactness can enable devices that can fit underneath clothing. This inconspicuousness will be a major improvement to overcome the stigmatization and low acceptance that these devices still have.

Acknowledgements

Funding

Declaration of Conflicting Interests

The authors report a pending patent application PA 2017 70789, filed on October 17th, 2017.

References

[1]   R.P. Paul, C.N. Stevenson, Kinematics of Robot Wrists, Int. J. Rob. Res. 2 (1983) 31–38. doi:10.1177/027836498300200103.

[2]   C. Carignan, J. Tang, S. Roderick, Development of an exoskeleton haptic interface for virtual task training, in: 2009 IEEE/RSJ Int. Conf. Intell. Robot. Syst., IEEE, 2009: pp. 3697–3702. doi:10.1109/IROS.2009.5354834.

[3]   S.J. Ball, I.E. Brown, S.H. Scott, MEDARM: a rehabilitation robot with 5DOF at the shoulder complex, in: 2007 IEEE/ASME Int. Conf. Adv. Intell. Mechatronics, IEEE, Zurich, Switzerland, 2007: pp. 1–6. doi:10.1109/AIM.2007.4412446.

[4]   J.C. Perry, J. Rosen, S. Burns, Upper-Limb Powered Exoskeleton Design, IEEE/ASME Trans. Mechatronics. 12 (2007) 408–417. doi:10.1109/TMECH.2007.901934.

[5]   Ho Shing Lo, S.S.Q. Xie, Optimization of a redundant 4R robot for a shoulder exoskeleton, in: 2013 IEEE/ASME Int. Conf. Adv. Intell. Mechatronics, IEEE, Wollongong, Australia, 2013: pp. 798–803. doi:10.1109/AIM.2013.6584191.

[6]   M.J.H. Lum, J. Rosen, M.N. Sinanan, Hannaford B, Kinematic optimization of a spherical mechanism for a minimally invasive surgical robot, in: IEEE Int. Conf. Robot. Autom. 2004. Proceedings. ICRA '04. 2004, IEEE, New Orleans, LA, USA, 2004: pp. 829–834. doi:10.1109/ROBOT.2004.1307252.

[7]   H.S. Lo, S.Q. Xie, Exoskeleton robots for upper-limb rehabilitation: State of the

art and future prospects, Med. Eng. Phys. 34 (2012) 261–268. doi:10.1016/j.medengphy.2011.10.004.

[8]   S. Christensen, S. Bai, Kinematic Analysis and Design of a Novel Shoulder Exoskeleton Using a Double Parallelogram Linkage, J. Mech. Robot. 10 (2018) 041008. doi:10.1115/1.4040132.

[9]   N. Sclater, N.P. Chironis, Mechanisms and Mechanical Devices Sourcebook, 4th ed., McGaw-Hill, New York, USA, 2007.

[10]   R.A.R.C. Gopura, K. Kiguchi, D.S. V Bandara, A brief review on upper extremity robotic exoskeleton systems, in: 2011 6th Int. Conf. Ind. Inf. Syst., IEEE, 2011: pp. 346–351. doi:10.1109/ICIINFS.2011.6038092.

[11]   A.G. Dunning, J.L. Herder, A review of assistive devices for arm balancing, in: 2013 IEEE 13th Int. Conf. Rehabil. Robot., IEEE, Seattle, Washington, USA, 2013: pp. 1–6. doi:10.1109/ICORR.2013.6650485.

[12]   F. Maden, K. Korkmaz, Y. Akgün, A review of planar scissor structural mechanisms: geometric principles and design methods, Archit. Sci. Rev. 54 (2011) 246–257. doi:10.1080/00038628.2011.590054.

[13]   G.E. Fenci, N.G. Currie, Deployable structures classification: A review, Int. J. Sp. Struct. 32 (2017) 112–130. doi:10.1177/0266351117711290.

[14]   C. Hoberman, Reversibly expandable doubly-curved truss structure, US4942700 A, 1990.

[15]   H. Kocabas, Gripper Design With Spherical Parallelogram Mechanism, J. Mech. Des. 131 (2009) 075001. doi:10.1115/1.3125891.

[16]   I.T. Watson, B. Gangadhara Prusty, J. Olsen, D. Farrell, A Parameter Investigation Into the Thompson Constant-Velocity Coupling, J. Mech. Des. 133 (2011) 124501. doi:10.1115/1.4005229.

[17]   H.S. Lo, S. Xie, Optimization and analysis of a redundant 4R spherical wrist mechanism for a shoulder exoskeleton, Robotica. 32 (2014) 1191–1211. doi:10.1017/S0263574714001945.

[18]   C.H. Chiang, Spherical kinematics in contrast to planar kinematics, Mech. Mach. Theory. 27 (1992) 243–250. doi:10.1016/0094-114X(92)90014-9.

[19]   C.H. Chiang, Kinematics of Spherical Mechanisms, 1st ed., Cambridge University Press, Cambridge, UK, 1988. https://books.google.dk/books/about/Kinematics_of_Spherical_Mechanisms.html?id=kVEOAAAACAAJ&redir_esc=y.

[20]   J. Denavit, R.S. Hartenberg, A kinematic notation for lower-pair mechanisms based on matrices, ASME J. Appl. Mech. 22 (1955) 215–221. doi:citeulike-article-id:7153318.

[21]   M. Ouerfelli, V. Kumar, Optimization of a spherical five-bar parallel drive linkage, J. Mech. Des. 116 (1994) 166–173. doi:10.1115/1.2919341.

[22]   J.J. Craig, Introduction to Robotics: Mechanics and Control, 3rd ed., Pearson Prentice Hall, NJ, USA, 2005.

[23]   T. Yoshikawa, Manipulability of Robotic Mechanisms, Int. J. Rob. Res. 4 (1985) 3–9. doi:10.1177/027836498500400201.

[24]   M.N. Castro, J. Rasmussen, S. Bai, M.S. Andersen, The reachable 3-D workspace volume is a measure of payload and body-mass-index: A quasi-static kinetic assessment, Appl. Ergon. 75 (2019) 108–119. doi:10.1016/j.apergo.2018.09.010.

[25] M. de Zee, L. Hansen, C. Wong, J. Rasmussen, E.B. Simonsen, A generic detailed rigid-body lumbar spine model, J. Biomech. 40 (2007) 1219–1227. doi:10.1016/j.jbiomech.2006.05.030.

[26] F.C.T. Van der Helm, H.E.J. Veeger, G.M. Pronk, L.H.V. Van der Woude, R.H. Rozendal, Geometry parameters for musculoskeletal modelling of the shoulder system, J. Biomech. 25 (1992) 129–144. doi:10.1016/0021-9290(92)90270-B.

[27] H.E.J. Veeger, F.C.T. Van Der Helm, L.H.V. Van Der Woude, G.M. Pronk, R.H. Rozendal, Inertia and muscle contraction parameters for musculoskeletal modelling of the shoulder mechanism, J. Biomech. 24 (1991) 615–629. doi:10.1016/0021-9290(91)90294-W.

[28] H.E.J. Veeger, B. Yu, K.-N. An, R.H. Rozendal, Parameters for modeling the upper extremity, J. Biomech. 30 (1997) 647–652. doi:10.1016/S0021-9290(97)00011-0.

[29] M.S. Andersen, M. Damsgaard, B. MacWilliams, J. Rasmussen, A computationally efficient optimisation-based method for parameter identification of kinematically determinate and over-determinate biomechanical systems., Comput. Methods Biomech. Biomed. Engin. 13 (2010) 171–183. doi:10.1080/10255840903067080.

[30] M.S. Andersen, M. Damsgaard, J. Rasmussen, Kinematic analysis of over-determinate biomechanical systems., Comput. Methods Biomech. Biomed. Engin. 12 (2009) 371–384. doi:10.1080/10255840802459412.

[31] H. Edelsbrunner, D. Kirkpatrick, R. Seidel, On the shape of a set of points in the plane, IEEE Trans. Inf. Theory. 29 (1983) 551–559. doi:10.1109/TIT.1983.1056714.

[32] D.B. Chaffin, G.B.J. Andersson, B.J. Martin, Occupational Biomechanics, 4th ed., Wiley, New Jersey, USA, 2006.

[33] J. Rosen, J.C. Perry, N. Manning, S. Burns, B. Hannaford, The human arm kinematics and dynamics during daily activities - toward a 7 DOF upper limb powered exoskeleton, in: ICAR '05. Proceedings., 12th Int. Conf. Adv. Robot. 2005., IEEE, Seattle, WA, United States, 2005: pp. 532–539. doi:10.1109/ICAR.2005.1507460.

[34] C.M. Gosselin, E. Lavoie, On the Kinematic Design of Spherical Three-Degree-of-Freedom Parallel Manipulators, Int. J. Rob. Res. 12 (1993) 394–402. doi:10.1177/027836499301200406.

[35] A. Schiele, F.C.T. van der Helm, Kinematic design to improve ergonomics in human machine interaction., IEEE Trans. Neural Syst. Rehabil. Eng. 14 (2006) 456–69. doi:10.1109/TNSRE.2006.881565.

[36] M.J.H. Lum, J. Rosen, M.N. Sinanan, B. Hannaford, Optimization of a spherical mechanism for a minimally invasive surgical robot: Theoretical and experimental approaches, IEEE Trans. Biomed. Eng. 53 (2006) 1440–1445. doi:10.1109/TBME.2006.875716.

[37] V. Vitiello, Su-Lin Lee, T.P. Cundy, Guang-Zhong Yang, Emerging Robotic Platforms for Minimally Invasive Surgery, IEEE Rev. Biomed. Eng. 6 (2013) 111–126. doi:10.1109/RBME.2012.2236311.